Investigation of flow characteristics of landslide materials through pore space topology and complex network analysis

Jia Zhang[1,2], Gang Ma[1,2], Zhibing Yang[1,2], Qirui Ma[3], Wenyu Zhang[1,2], Wei Zhou[1,2]

[1] State Key Laboratory of Water Resources and Hydropower Engineering Science, Wuhan University, Wuhan 430072, China.

[2] Key Laboratory of Rock Mechanics in Hydraulic Structural Engineering of Ministry of Education, Wuhan University, Wuhan 430072, China.

[3] Changjiang Institute of Survey, Planning, Design and Research, 430010, Wuhan, China.

Corresponding author: M. Gang (magang630@whu.edu.cn)

Key Points:

- Conventional topological measures except tortuosity fail to explain the influence of pore structure on flow characters in low permeability.
- The relationship between permeability and throat diameter spanning nine orders of magnitude is consistent with the Hagen–Poiseuille theory.
- Complex network theory is proven useful to unveil the topological characteristics of pore networks.

Abstract

Unlike embankments, earth dams, and other man-made structures, most landslide dams are formed by rapid accumulation of rock or debris rather than mechanical compaction; thus, they are loose and pose a great risk of seepage failure. Landslide materials usually have complex pore structures with randomly distributed pores of various sizes, making the flow and transport processes very complex. Aiming at these challenges, we have studied the influences of pore structure on the micro-and macro-scale flow characteristics of landslide materials. First, landslide materials are simplified as spherical granular packings with wide grain size distributions. Then, we use finite difference method (FDM) and lattice Boltzmann method (LBM) to simulate the fluid flow through granular packings and calculate their permeability. We find that both the correlation between pore-scale velocity and throat diameters and the correlation between macroscopic permeability and average throat diameters follow a power-law scaling with an exponent close to 2, in agreement with the Hagen–Poiseuille equation for laminar flow in pipes, suggesting that the relationships in complex pore structures are conformed with the simple theory. Moreover, we propose a new method by combining pore networks and complex networks to characterize the pore structure. The network analysis illustrates that granular packings with different permeability display distinctive distributions of pore throat size and pore connectivity and their correlations. Compared with disassortative pore networks, assortative ones generally have higher permeability. Furthermore, pores with larger closeness centrality have higher flow efficiency that results in higher macroscopic permeability.

1 Introduction

Landslide dams are common worldwide, especially in tectonically active mountain regions, which are usually caused by natural hazards, such as mountain collapse, earthquakes, and mudslides. Landslide dams are mainly composed of loose soil and fragmented rocks with grain size spanning several orders of magnitude (Sun et al., 2016). The blockage of river channels by landslide dam results in raising water in upstream areas. With the increase of water level in dammed lake, the loose dam body will collapse catastrophically, causing anomalous destructive flood waves and posing a significant threat to downstream life and properties (Peng & Zhang, 2012). Therefore, the study of landslide dams and their consequences has acquired significant relevance in scientific research to predict and prevent landslide dam collapse. Many factors influencing the stability of landslide dam have been studied comprehensively, such as dam

geometry (Chen et al., 2015), grains composition (Okeke & Wang, 2016), the angle of dam downstream face (Gregoretti et al., 2010) and permeability, which is considered as one of the critical factors affecting the stability of landslide dam (Costa & Schuster 1988).

Previous studies on the hydraulic properties of landslide materials through experimental and field tests (Okeke & Wang, 2016) and numerical simulations (Zhu et al., 2020) have revealed that the grain size distribution of the dam accumulation has significant impacts on the seepage stability of landslide dams. However, the relationship between pore structure and hydraulic properties of landslide materials has not been fully understood, mainly due to the difficulties of characterizing the pore structure of landslide materials. The complex pore structure is originated from the quick deposits of landslide materials composed of poorly graded soils and fragmented rocks. The existing test results have shown 1~2 orders of magnitude permeability variation for approximately the same porosity. This variation has been attributed to the complex pore structure of landslide materials (Miller et al., 2015; Thomson et al., 2018).

Characterization of the pore structure is of great interest in many scientific and technological areas. Many techniques have been developed to examine the pore space of porous medium, such as scanning electron microscopy (SEM) (Peters, 2009), mercury injection capillary pressure (MICP) (Xiao et al., 2016), nuclear magnetic resonance (NMR) (Li et al., 2021), and X-ray (Zambrano et al., 2019). By the aid of the nondestructive and quantitative methods, the inhomogeneity coefficient, curvature coefficient, critical pore radius (Nishiyama & Yokoyama, 2017), tortuosity (Ahmadian et al., 2019) have been used to characterize the microscopic pore structure and link to macroscopic permeability. On the numerical modeling side, several pore-scale methods have been widely used, such as the pore network model (PNM) (Dong & Blunt, 2009; Fatt, 1956). The PNM and its variants have been extensively used in characterization of pore space geometry and topology as well as simulation of multiphase and single-phase flows in porous media (An et al., 2016; Esmaeilpour et al., 2021; Steinwinder & Beckingham, 2019; Zhang et al., 2019).

Besides the pore throat size distribution, the pore connectivity and pore spatial distribution have been found to play important roles in fluid flow through porous media (Cai et al., 2019). Pore connectivity can be quantified by either coordination number (Thomson et al., 2018) or connectivity factor (Cai et al., 2019; Hunt, 2004). Coordination number can be evaluated by medial axis analysis, which reduces the macropore space to a medial axis and calculates the average

number of branches at a junction (Hormann et al., 2016). Recently, Zhang et al. (2021) extracted the pore networks from samples slices and proposed two connectivity indexes based on generated pseudo MICP curves to evaluate the connectivity of 2D pore networks quantitatively. Bernabé et al. (2010) proposed a new model based on network simulations and percolation theory and highlighted the importance of pore connectivity and pore size heterogeneity on fluid flow in porous media (Bernabé et al., 2011).

Despite the advances in previous studies, there is a lack of detailed analysis on robust multiscale descriptors of pore connectivity and their relationship to fluid flow characteristics (Bernabé et al., 2010; Cai et al., 2019). Complex network analysis provides a new perspective to study pore connectivity and the multiscale characterization of pore network. For example, Van Der Linden et al. (2016) developed a framework to characterize the internal pore structure and fluid transmission efficiency of porous media using complex network theory; by combining the particle's complex network and its pore network, Russell et al. (2016) proposed a framework to characterize the coupled evolution for planar deformation considering the geometry and connectivity of pores; Jimenez-Martinez and Negre (2017) proposed an measure called eigenvector centrality based on complex network theory to characterize the geometric and topological characterization of porous media; Valera et al. (2018) developed an approach to describe transport in fractured rock based on node centrality of complex network.

This study aims to develop a framework to investigate the effect of pore structure on microscale flow characteristics and macroscopic hydraulic properties of landslide materials. Because the landslide materials are very complex and the grain size exceeds the limitation of current experimental techniques, we simplify the landslide materials as granular packings and perform a large set of numerical simulations. The workflow of this study is shown in **Figure 1**. We firstly generate granular packings with different grain size distributions to represent typical landslide materials. Then, the pore space of the granular packing is extracted, and the fluid flow through granular packing is numerically simulated. Finally, the pore space topology, pore network model, and complex network analysis are used to link the pore structure and micro- and macroscopic flow characteristics of landslide materials.

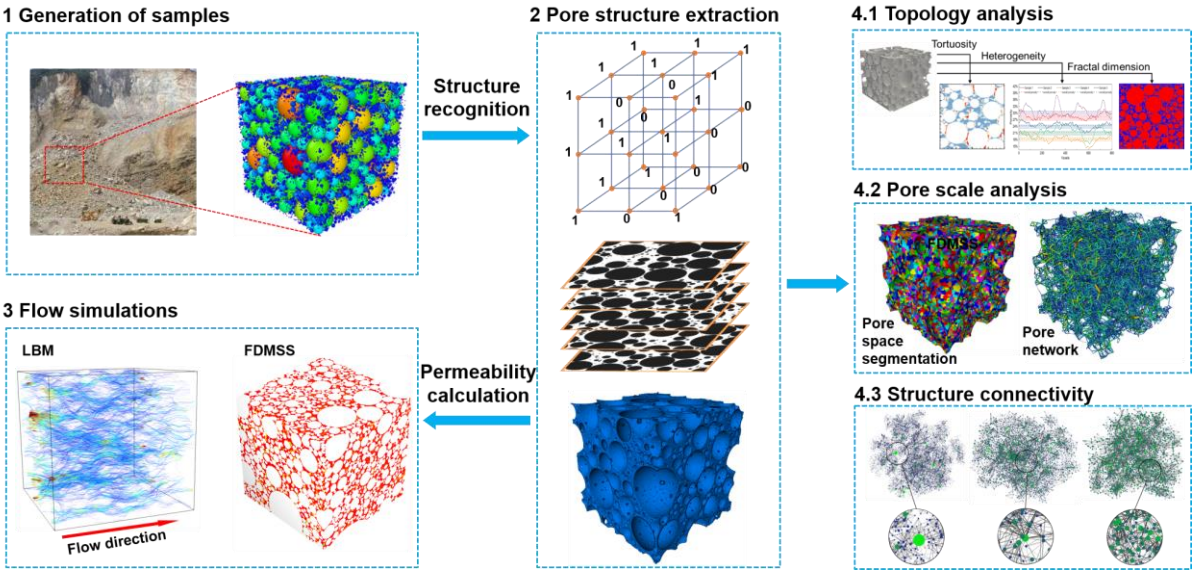

Figure 1 Workflow of this study.

2 Permeability evaluation of landslide deposits

2.1 Typical samples of landslide deposits

We collected grain size distributions (GSDs) of 32 landslide dams located all over the world. As shown in **Figure 2a**, the GSD of natural landslide deposits varies significantly. With the increase of fine grains, the grain gradation curve gradually changes from a convex shape to a concave one. In this study, we select seven GSDs to represent the typical landslide deposits. Samples 1 and 2 have more fine grains; Samples 4~7 have more coarse grains; Sample 3 is characterized by a relatively uniform size distribution.

The discrete element method (DEM) was used to generate the widely graded granular packings shown in **Figure 2b**. The grain diameter ranges from 2 mm (d_{min}) to 80 mm (d_{max}) following the distributions illustrated in **Figure 2a**. Firstly, loose assemblies of nonoverlapping grains with a dimension of 0.4×0.4×0.4 m were generated randomly. Then, the grain assemblies were triaxially compressed to an equilibrium state under the confining pressure of 1MPa (Ma et al., 2016). The input parameters for the DEM simulations of granular packing are summarized in **Table 1**.

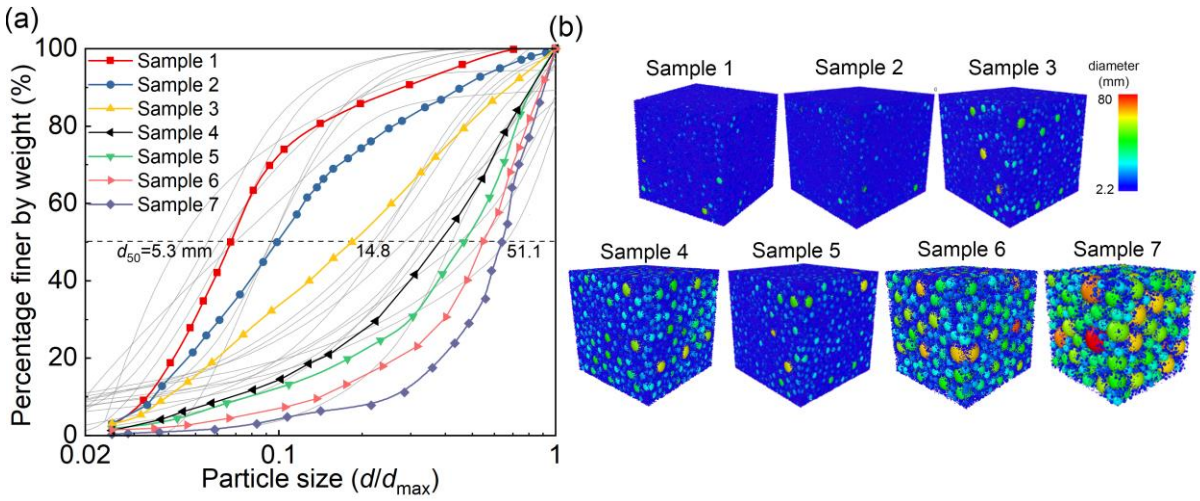

Figure 2 (a) Grain size distributions collected from 32 landslide dams (grey color) and seven GSDs used in this study (colored lines); (b) Granular packings with different GSDs and particles are colored by their diameter.

Table 1 Input parameters for DEM simulation of granular packing

Parameters	Symbol	Units	Values
Grain density	ρ	kg/m^3	2600
Young's module	E	GPa	65
Timestep	Δt	s	1e-7
Initial size of samples	H	m	0.4
Target confining pressure	P	MPa	1
Poisson ratio	ν	-	0.2
Friction	μ	-	0.1
Contact model		-	Hertz-Mindlin

2.2 Fluid flow simulation using FDMSS

Take one granular packing as an example, the granular packing was divided into 1000×1000×1000 voxels, as shown in **Figure 3a**. The voxel size is approximately 0.3 mm, about 1/7 of the smallest grain. To extract the pore space, we converted 1000×1000×1000 voxels into a three-dimensional matrix according to grain position and grain size, in which each element has a

value of either 0 (void voxel) or 1 (solid voxel). **Figure 3b** and **Figure 3c** show the pore space extracted from the granular packing and several fluid streamlines for illustration. The finite-difference method Stokes solver (FDMSS) is used to simulate the fluid flow (Gerke et al., 2018). The FDMSS uses the finite difference method to directly solve the Navier-Stokes equation, which has been verified and proven to be efficient and accurate. Compared with other methods, such as classic FDM (Shabro et al., 2012) and LBM (Khirevich et al., 2015), FDMSS has higher accuracy and convergence speed and lower computational cost. The interested readers may refer to Gerke et al. (2018) for the details of FDMSS.

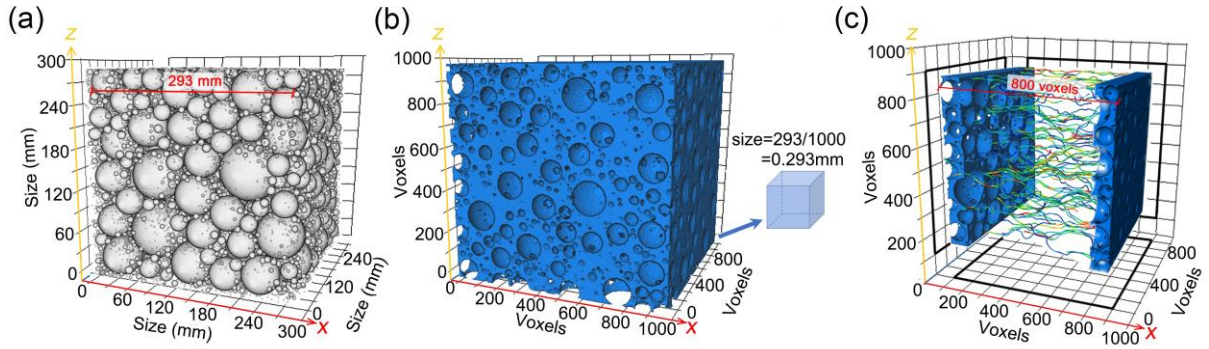

Figure 3 (a) Granular packing; (b) Extraction of pore space; (c) Illustration of the fluid flow paths.

Flow velocity fields are modeled by applying pressure gradients across three principal directions while treating all other sides of the granular packing as impermeable walls (see **Figure 4a**). The permeability along flow direction can be calculated using Darcy's equation $K = \mu LQ/(\Delta pS)$, where μ is fluid viscosity, L is the distance of fluid flow, Q is flow rate, Δp is pressure difference between inlet and outlet boundaries, and S is the cross-sectional area. To eliminate the boundary effects on fluid flow simulation, a subset of manually binarized images was cropped from the original stack for simulations resulting in 3D modeling domains containing 300^3~800^3 voxels. The representative volume element (RVE) is obtained when the measured or calculated permeability plotted versus increasing sample size reaches a plateau (**Figure 4b**). Meanwhile, grid sensitivity analysis is also performed (**Figure 5**). It can be seen that the permeability becomes stable when the resolution is less than 0.35 mm/voxel. Thus, the resolution

we choose is accurate enough for the flow simulations. The granular packing porosity ϕ, mean grain size d_{50}, permeability calculated by FDMSS K_{FDMSS} are summarized in **Table 2**.

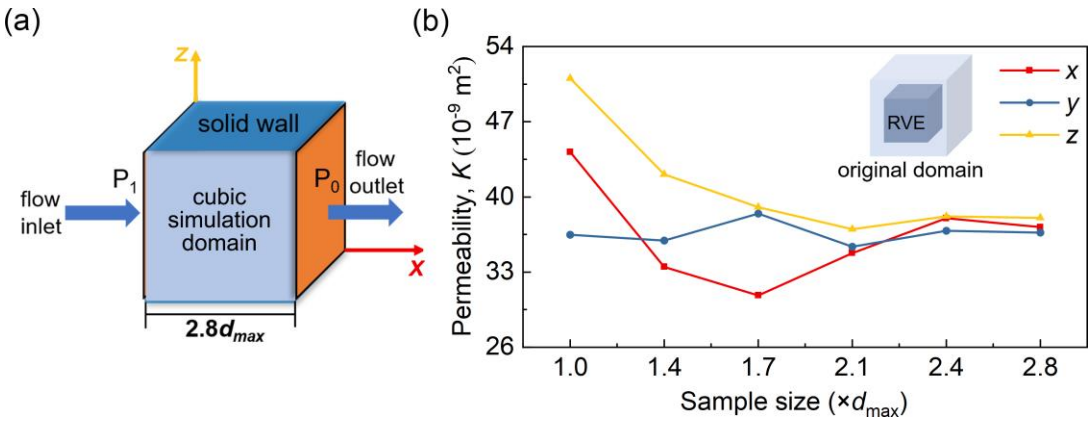

Figure 4 (a) Simulation domain and boundary conditions of the fluid flow simulation; (b) RVE size effect on the permeability of granular packing.

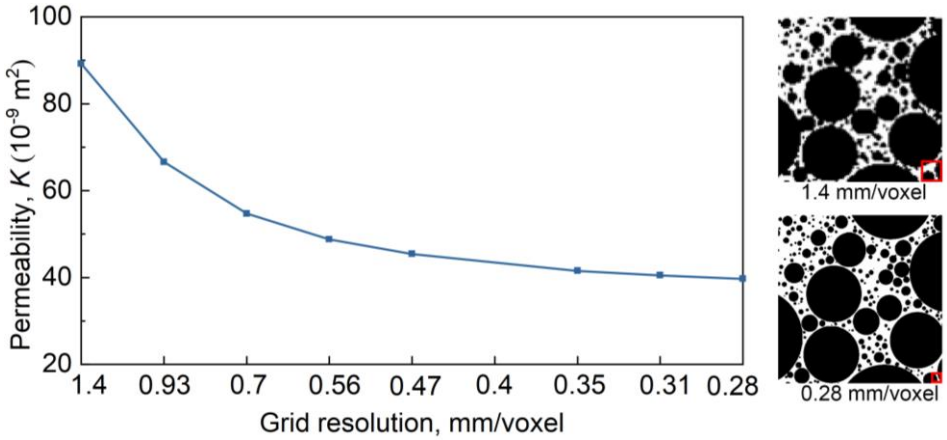

Figure 5 Grid sensitivity analysis (The lattice number is 200^3 ~1000^3 corresponding to the resolution of 1.4~0.28 mm/voxel).

Table 2 Basic information of the granular packings and their permeability

	Porosity ϕ	d_{50} (mm)	Permeability K_{FDMSS} ($\times 10^{-9}$ m^2)	Range
Sample 1	0.29	5.33	5.15	
Sample 2	0.24	7.81	4.73	$1< K <10$
Sample 3	0.19	14.84	3.65	
Sample 4	0.19	30.80	16.49	
Sample 5	0.22	37.28	39.70	$10< K <100$
Sample 6	0.26	43.73	76.77	
Sample 7	0.31	51.13	306.27	$K >100$

The permeability of the seven granular packings covers nearly two orders of magnitude. We can divide the granular packings into three categories according to their permeability to facilitate the following analysis. Sample 2, Sample 5 and Sample 6 have the similar porosity, but they show an order of magnitude difference in permeability. Sample 3 and Sample 4 have the same porosity, but display a distinct difference in permeability. This means that the porosity alone cannot reflect the effect of pore structure on permeability. Therefore, a more thorough investigation of the effect of pore structure on flow characteristics of landslide materials is necessary. Besides FDMSS, we also use LBM to simulate the fluid flow through the porous space. The LBM simulation with the D3Q19 lattice model achieves a good balance between stability and efficiency. The permeabilities calculated by FDMSS and LBM are nearly the same. However, the computational efficiency of FDMSS is much higher than that of LBM.

2.3 Construction of pore-throat structure and complex network

The pore space topology of the granular packing is analyzed by the pore network model (PNM) and complex network approach, respectively. The pore network of the granular packing is extracted using the maximal sphere method developed by Dong & Blunt (2009). According to the maximal sphere algorithm, the pore space is divided into pore bodies and throats. Then the PNM consisting of the network of pores and throats is constructed, in which throats are the local constrictions that connect the adjacent pores. The pore network model provides an effective way of analyzing the geometry and topology of the pore space. The topology and geometry information

about the pore structures of granular packings are summarized in **Table 3**. Using Sample 3, Sample 5 and Sample 7 as examples, we show the pore space and pore network model of these three granular packings in **Figure 6**. It is clear that the pore network of Sample 3 is relatively concentrated, while Sample 5 and Sample 7 are relatively loose, indicating the pore distribution is scattered and coarse.

Table 3 Parameters of different samples simulated by the pore network modeling

	Sample 1	Sample 2	Sample 3	Sample 4	Sample 5	Sample 6	Sample 7
Size (mm)	283	278	272	273	278	282	293
Pores number	79396	59739	40226	10718	6615	3846	1692
Throats number	428315	297364	184380	45815	28075	16079	6765
Average pore connection number	10	10	9	8	8	8	8
Max pore connection number	45	39	35	25	21	20	21
Average pore diameter (mm)	1.77	1.81	1.82	2.78	3.75	5.17	8.21
Max pore diameter (mm)	4.00	3.90	3.91	6.00	8.84	10.53	14.39
Average pore volume (mm^3)	10.12	11.42	12.42	48.88	98.06	208.90	647.27
Max pore volume (mm^3)	115.00	103.61	154.79	497.49	944.09	1866.88	4516.30
Average throat diameter (mm)	0.94	0.97	0.99	1.52	2.04	2.84	4.54
Max throat diameter (mm)	3.20	3.31	3.36	5.44	7.31	8.21	13.41
Average throat volume (mm^3)	5.89	6.78	7.62	31.29	62.73	136.19	424.52
Max throat volume (mm^3)	110.33	124.44	166.62	434.58	851.76	2018.39	5514.10
Average throat length (mm)	7.30	7.42	7.48	10.69	12.87	15.57	21.39
Max throat length (mm)	24.51	24.30	27.40	30.63	37.28	45.78	58.60

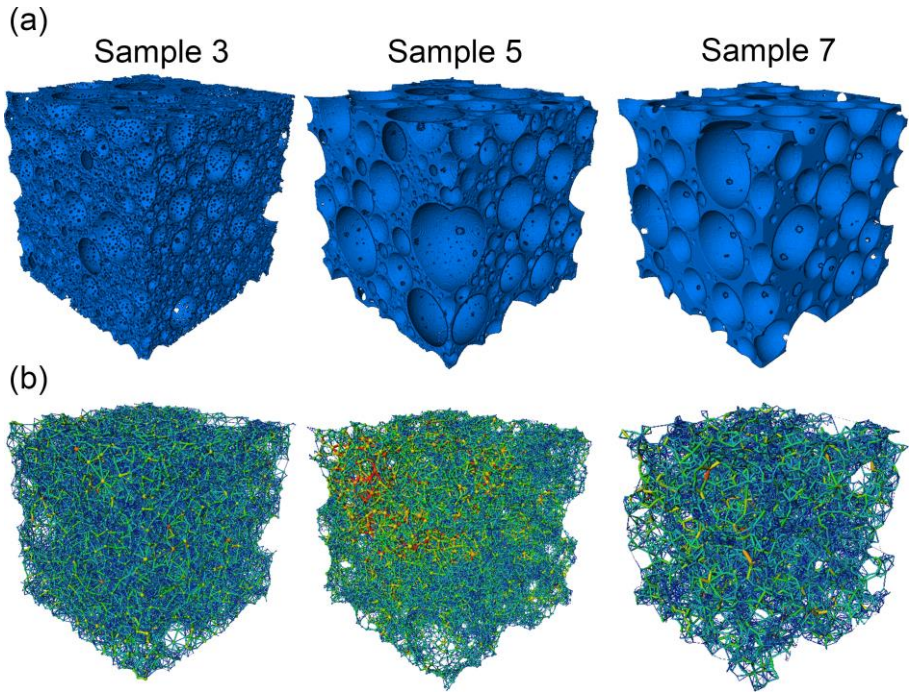

Figure 6 (a) Pore space and (b) Pore throat network of three typical granular packings.

3 Topological characteristics of pore structure

Landslide materials are highly complex systems characterized by significant variability of grains and pore sizes. Although landslide materials have been idealized as spherical granular packing with different GSDs, their internal structures are significantly different due to the significant differences in the GSD of the granular packings. It has been well recognized that the fluid flow in porous media is affected by its internal structure (Alim et al., 2017). In this section, we use several measures to characterize the topological properties of the pore structure.

3.1 Conventional topological measures

Tortuosity is an intrinsic property of a porous material usually defined as the ratio of actual flow path length to the straight distance between the ends of the flow path (Ghanbarian et al., 2013). It has been reported that tortuosity is an important factor affecting flow and transport in porous media (Cai et al., 2019). As the tortuosity τ becomes larger, the flow path will be more tortuous and longer. We first show how tortuosity affects the permeability of landslide materials. Instead of using its geometric definition, we calculate the tortuosity using the velocity vector of the flow field. The tortuosity along the flow direction (*x*-direction) is defined as:

$$\tau_x = \frac{\sum_{i=1}^{N} \sqrt{v_{xi}^2 + v_{yi}^2 + v_{zi}^2}}{\sum_{i=1}^{N} v_{xi}} \quad (1)$$

Where τ_x is the tortuosity in the x-direction; the subscript i denotes the i-th node in the flow field; N is the total number of nodes in the flow field; v_{xi}, v_{yi}, and v_{zi} are the *x*, *y*, and *z* components of the velocity vector. The local tortuosity at each node can be calculated analogically as $\tau_{xi} = \sqrt{v_{xi}^2 + v_{yi}^2 + v_{zi}^2} \Big/ v_{xi}$.

The relationship between tortuosity and permeability is plotted in **Figure 7**. Although the permeability spans eight orders of magnitude, these data points collapse to a master curve with a determination coefficient of 0.99. The permeability demonstrates a decreasing trend with the increase of tortuosity, which is consistent with previous studies (Nishiyama & Yokoyama, 2017; Zambrano et al., 2019). We then analyze the influencing mechanism of tortuosity on permeability. As shown in **Figure 8a**, the curvature of the streamlines gradually decreases due to the increase of coarse grains in the granular packing. Take Sample 7 as an example, coarse grains take up most of the space, and large pore space is generated without the filling of fine grains. Therefore, there is no obstruction of fine grains when the fluid flows, leading to straight flow path and high flow velocity between large pores (**Figure 8b**). With the increase of fine grains, local blocking structures are formed by the filling of fine grains. Thus, due to the more tortuous flow paths, the fluid flow through the porous media becomes difficult and results in lower permeability. **Figure 8c** shows the local tortuosity at the cross-section of the three granular packings. As shown, the front and rear regions of pores show higher tortuosity. Therefore, the porous media consisting of more pores display a higher tortuosity, which explains the relationship between permeability and tortuosity.

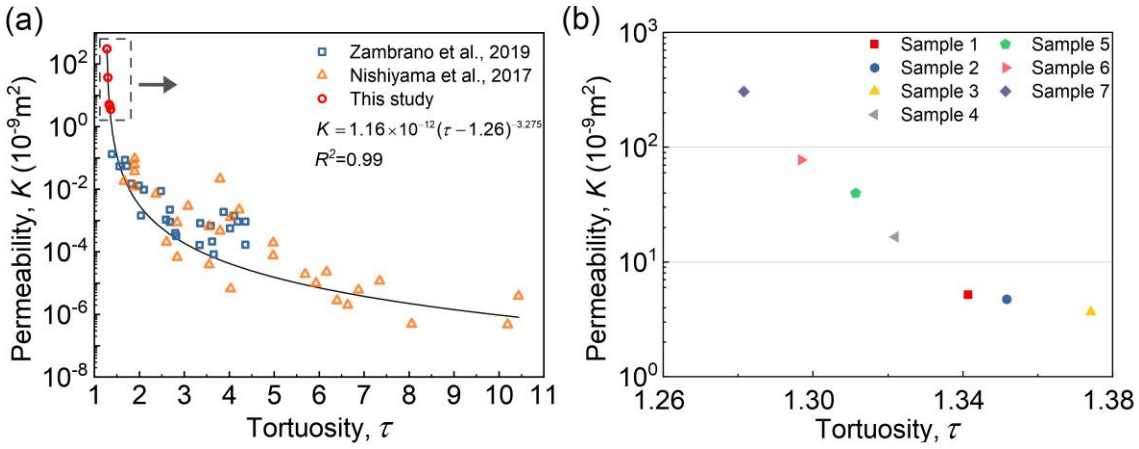

Figure 7 The relationship between tortuosity and permeability. The right panel (b) is an enlarged view of the dotted box shown in (a).

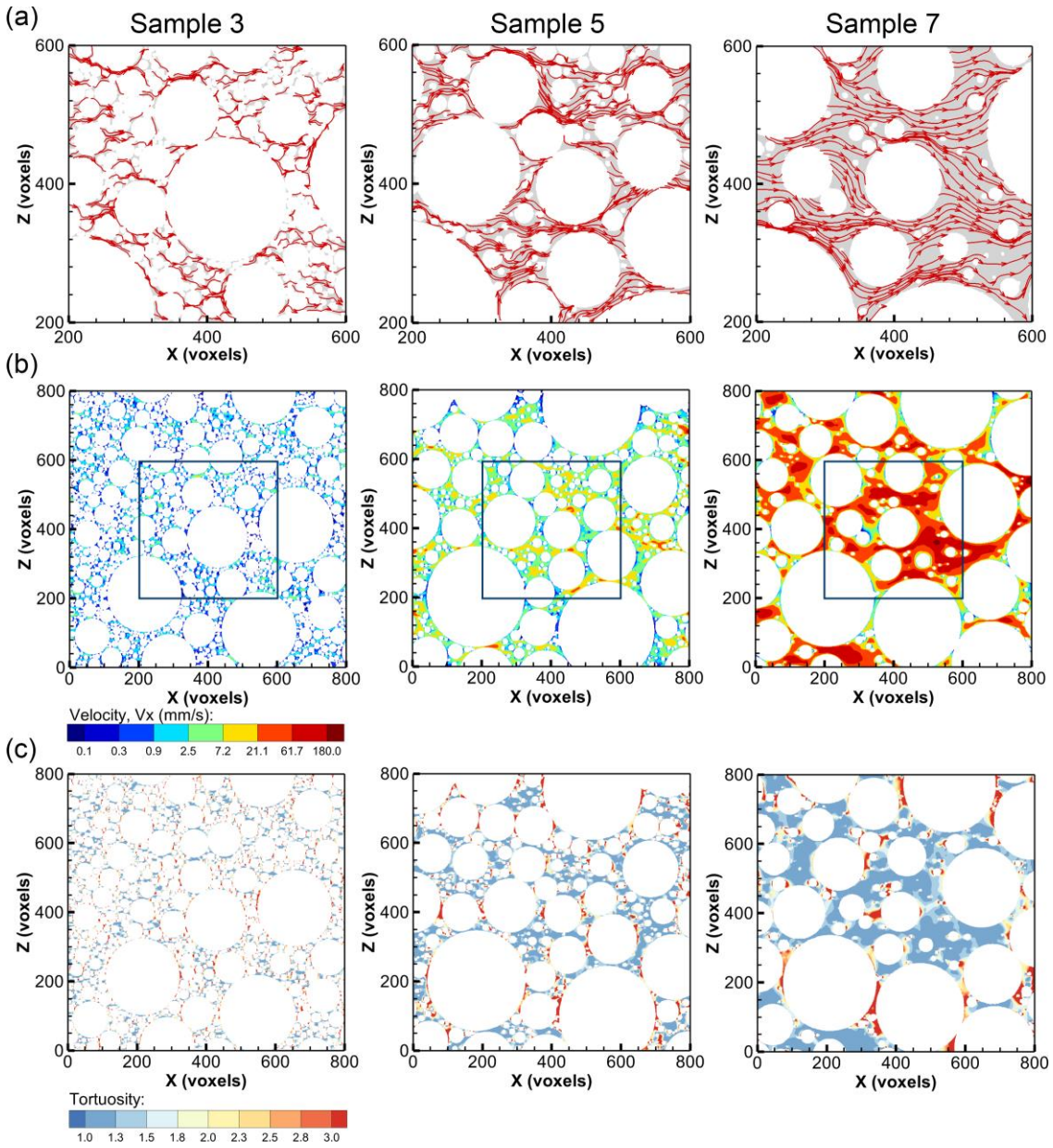

Figure 8 The distributions of (a) Streamline, (b) Flow velocity, and (c) Tortuosity of each node at the cross-section of the three typical granular packings.

Disorder is another intrinsic property of porous media, which profoundly influences the stress transmission and failure (Huang et al., 2021; Zaiser, 2017), flow and transport characteristics (Zami-Pierre et al., 2018). The disorder of porous media can be manifested as the heterogeneity of pore size distribution or local porosity distribution. Porous media with non-uniformly distributed pore size and local porosity generally have a higher degree of disorder. As suggested by Laubie (2017), the domain containing the granular packing is divided into several subdomains to facilitate

the calculation of local porosity (see **Figure 9a**). A heterogeneity index can be defined as the standard deviation of the local porosity of each subdomain (Laubie, Radjai, et al., 2017; Wang et al., 2016).

$$I_d = \sqrt{\langle \phi_i^2 \rangle - \phi^2} \tag{2}$$

where I_d is the heterogeneity index, ϕ is the global porosity of the granular packing, and ϕ_i is the local porosity of the *i*-th subdomain.

The relationship between pore heterogeneity and permeability is plotted in **Figure 9b**. The permeability shows an overall increasing trend with I_d in samples 4~7, suggesting that granular packings with the increasing of coarse grains showing more obvious pore aggregation have higher permeabilities. However, the heterogeneity does not display an obvious trend when the proportion of fine grains is large (as in Samples 1~3). This means that I_d is determined by the GSD when there are more coarse grains in samples, but it is not applicable to the samples composed of more fine grains.

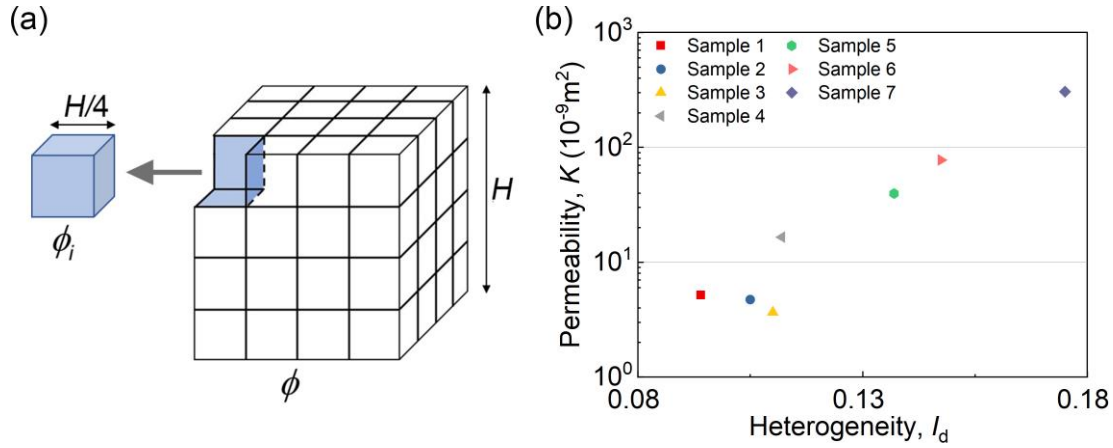

Figure 9 (a) Illustration of the pore heterogeneity calculation; (b) The relationship between heterogeneity and permeability.

Besides tortuosity and heterogeneity, we further use fractal dimension to characterize the pore space topology. Many studies have shown that the pore space of porous media has a typical fractal structure (Yu & Cheng, 2002; Yun et al., 2009). The fractal dimension of the pore space is calculated using the box-counting method (see **Figure 10a**). The overall tendency is that the fractal

dimension increases with the increasing proportion of fine grains in porous media with low permeability (**Figure 10b**). The fractal dimension does not appear to be a robust metric to describe the pore structure for characterization of hydraulic properties; e.g., samples 1~3, having a similar permeability, display quite different fractal dimensions. Therefore, we propose a new method based on microscopic analysis with pore networks and complex networks in Section 4 and 5.

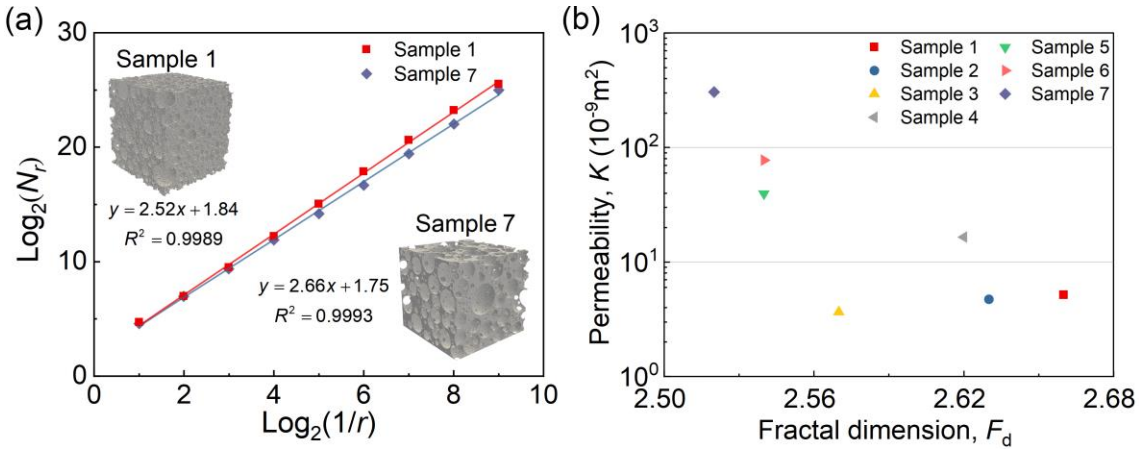

Figure 10 (a) Illustration of the calculation of fractal dimension of pore space; (b) The relationship between fractal dimension and permeability.

3.2 Characterization of the complex pore network

This section focus on analyzing the topological characteristics of pore structure using the complex network theory (Papadopoulos et al., 2018). A complex network is a graph, which can help to simplify the pore structure and give insights into the flow and transport properties in porous media (Jimenez-Martinez & Negre, 2017; Van Der Linden et al., 2016, 2019). As shown in **Figure 11**, a complex network is constructed to represent the pore throat network, in which the nodes represent pores (centroid of the pore) and edges represents throats determined by the medial axis method. In order to relate the complex network features to the flow characteristics of porous media, some studies constructed weighted complex network to represent the pore throat structure. Different choices of edge weight have been proposed, such as conductance (Van Der Linden et al., 2016) and throat cross-section area (Jimenez-Martinez & Negre, 2017).

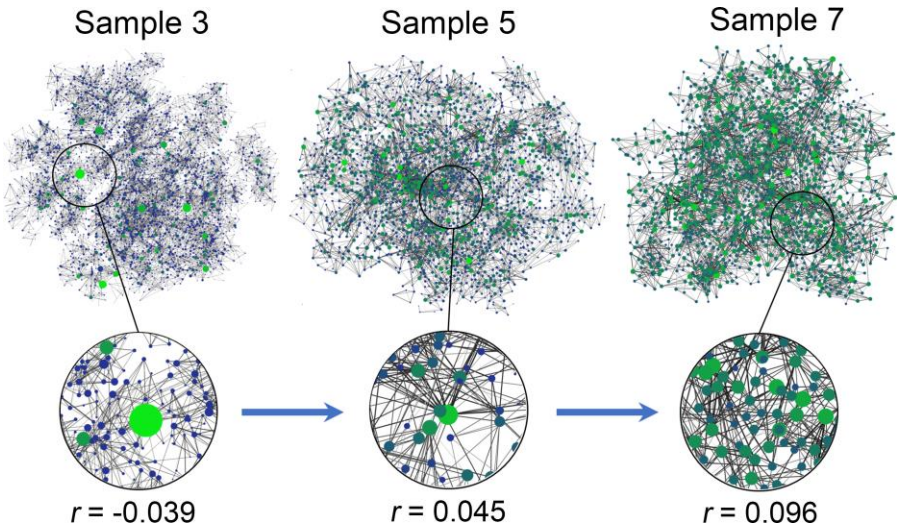

Figure 11 Complex network representation of the pore structure of three typical granular packings. *r* is the degree correlation coefficient. complex networks tend to be assortative with the increase of *r*.

The complex network constructed in this way is physically representative and can be viewed as a "fingerprint" of the porous media. The complex pore network is denoted as a graph $G=(V, E)$, where $V=\{1,\ldots,N\}$ is the set of nodes (pores) and $E \subseteq V \times V$ is the set of edges that represents throats. We use several overall network features to characterize the transport efficiency and flowing capacity in the network, such as global efficiency, entropy, and transitivity. The global efficiency represents the average of the reciprocal path lengths of all nodes in the complex network and can be interpreted as a measure of how well the flow is transmitted through a network. The global efficiency $\bar{E}_{glob}$ is defined as:

$$\bar{E}_{glob} = \frac{1}{N(N-1)} \sum_{i,j} \frac{1}{d_{ij}} \tag{3}$$

where N is the number of nodes; d_{ij} is the shortest path length between node *i* and *j*, representing the shortest number of steps necessary to get from node *i* to *j*. The flow transmission rate is dependent upon d_{ij}, and lower d_{ij} corresponds to higher transmission efficiency.

The entropy of degree distribution is an important concept that measures the node connection inhomogeneity in the complex network (Reichl & Luscombe, 1999). It is defined as:

$$H = -\sum_{k} P(k) \log P(k) \tag{4}$$

Where k is the degree that represents the number of edges connected to a node; $P(k)$ is the fraction of nodes in a network with degree k. The entropy achieves the maximum value when the degree distribution is uniform (wide), and the minimum value of entropy is 0 when the nodes have the same degree.

The transitivity is defined by the fraction of all possible triangles present in the graph (Zlatić et al., 2012). Possible triangles are identified by the number of triads composed of two edges with a shared node. Suppose that a node i has k_i neighbors. The maximum number of edges are $k_i(k_i - 1)/2$. The transitivity can be calculated as:

$$T = \frac{3t(G)}{\sum_{i \in V} \frac{k_i(k_i - 1)}{2}} \tag{5}$$

Where $t(G)$ is the number of triangles in G; k_i is the degree of node i. The transitivity reflects the probability that two random neighbors of one node are neighbors with each other and can be used to measure how well nodes tend to be clustered.

As shown in **Figure 12a**, the network with higher global efficiency has better flow transmission efficiency, thus, demonstrating larger permeability. Specifically, in Samples 1~3, the nodes that are not close to one another are separated by multiple edges and have longer path length, therefore, the connectivity between nodes is weakened. In Samples 4~7, the length of the shortest path connecting two nodes is shorter, and the fluid can reach another node through fewer edges. Thus, the fluid can communicate, transform, and transmit in each node with greater efficiency, which ultimately lead to higher permeability. With the increase of fine grains, the entropy reflecting the node connection inhomogeneity increases. The complex networks with higher entropy demonstrate lower permeability (see **Figure 12b**). The networks with larger transitivity also display higher permeability (see **Figure 12c**). We can conclude from this analysis that granular packings with relatively clustered pores that are linked by high connectivity throats have high permeability.

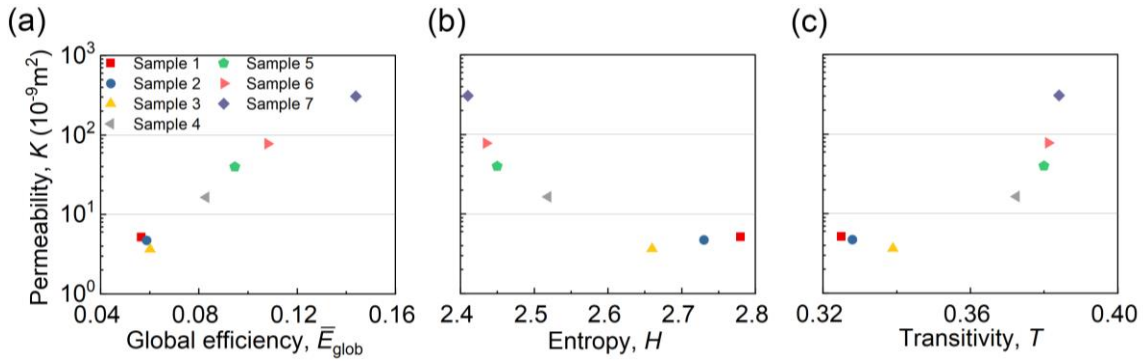

Figure 12 The relationships between permeability and three complex network features: (a) Global efficiency; (b) Entropy; (c) Transitivity.

4 Microscopic investigation by pore network analysis

The above analysis indicates that both conventional topological parameters and complex network measures can be used to investigate the relationship between pore structure and permeability at the macroscopic scale. Among these metrics, tortuosity and global efficiency perform better than others. We further investigate the relationship between the microscopic pore structure and pore scale flow dynamics. In this section, the pore and throat geometry obtained from PNM are analyzed in detail. We mainly focus on the pore and throat size distributions of different granular packings and their correlations with pore connectivity and flow dynamics.

Using Sample 3, Sample 5 and Sample 7 as typical examples, the distributions of pore size and pore coordination number and their correlations of different granular packings are shown in **Figure 13**. The pore connection number represents the number of throats connected to a pore. With the increase of coarse grains, the pore size gradually increases and varies in a wider range. The connection number increases with increasing pore size, indicating that larger pores tend to connect more throats. In Sample 3, the pore sizes scatter in a quite narrow range, while the pore connection numbers show a relatively wide range. Thus, the relationship between pore size and pore connection number is fitted by a line with a larger slope, indicating that small pores with few connection numbers are more likely to link to large pores with multiple connection numbers.

The distributions of throat diameter and throat length and their correlations of different granular packings are presented in **Figure 14**. It clearly outlines the positive correlation between pore throat size and permeability, suggesting that longer and larger throats generally result in higher permeability of granular packing. With the increase of fine grains, the void space can be

filled by finer grains, the cross-section area of throat becomes smaller, which hinders the flow in granular packing. As the proportion of coarse grain increases, the granular packing tends to generate large void space without filling of finer grains, therefore, the pore space are manifested by larger pore and throat size with relatively evenly distributed connection number. We can categorize the granular packings into three groups according to the features of the pore throat geometry and their correlations. The significant difference in pore throat geometry and their connectivity results in permeability difference of orders of magnitude.

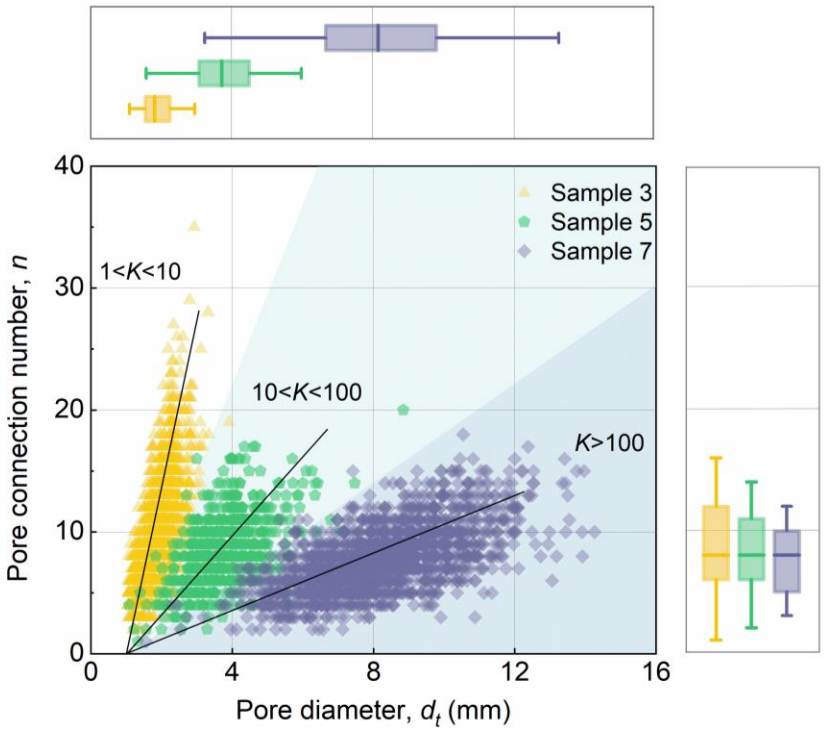

Figure 13 Scatter plot of pore diameter and pore connection number with marginal boxplots of different granular packings (Permeability K, 10^{-9} m^2).

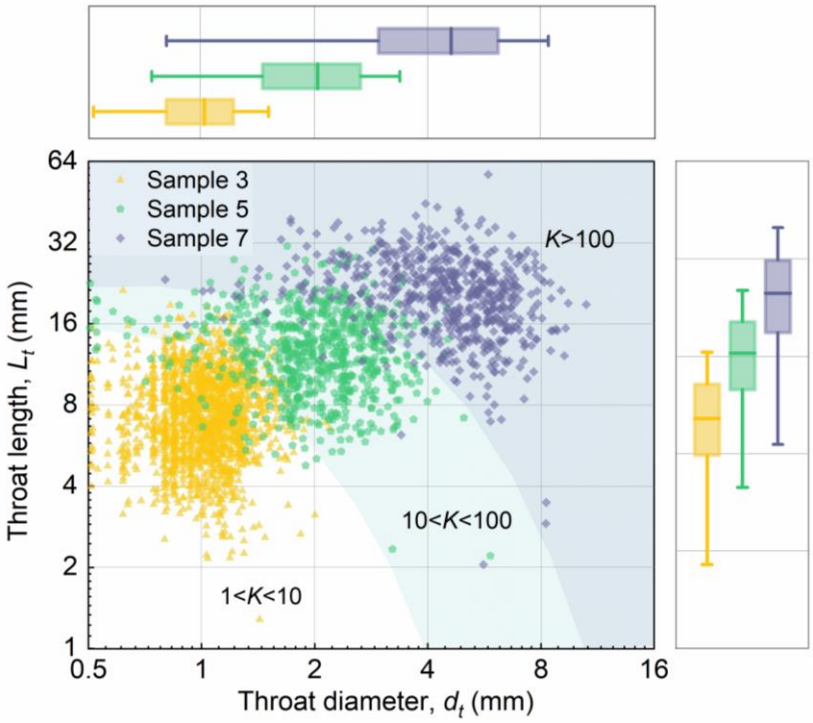

Figure 14 Scatter plot of throat diameter and throat length with marginal boxplots of different granular packings (Permeability K, 10^{-9} m^2).

The correlations between pore throat geometry and flow characteristic are also analyzed at both the pore scale and the macroscale. The flow velocity at the throat center is plotted as the function of throat diameter (**Figure 15a**). At the pore scale, the flow velocity increases approximately linearly with throat diameter in the log-log scales with a slope of about 2.2, i.e. $V_x \propto d_t^{2.2}$, which is in close agreement with Hagen–Poiseuille equation: the velocity of the fluid is proportional to the square of the pipe diameter. This demonstrates that the relationship between velocity and throat diameter in complex porous media is basically conformed with the simple theory. At the macroscopic scale, we observe a strong correlation between the average throat diameter and macroscopic permeability of various porous media. The data points from different sources (Encalada et al., 2020; Lala & El-Sayed, 2017; LU et al., 2018; Pang et al., 2018) collapse onto a single master curve shown in **Figure 15b**. The slope of the fit is 2.18, which is basically in accordance with the results of $K \propto D^2$ by combining the Hagen-Poiseuille equation and Darcy's Law (Ozgumus et al., 2014). This indicates that there are strong connections between the pore

structure and the fluid flow characteristics, and that the connections exist at both micro-and macro-scales.

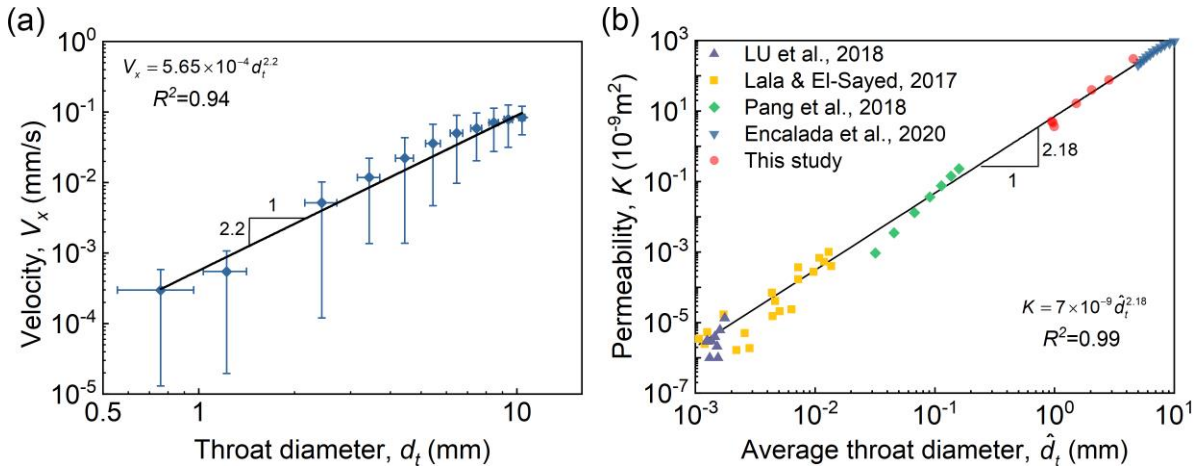

Figure 15 (a) The relationship between throat diameter and pore-scale velocity plotted with error bars (b) The relationship between average throat diameter and macroscopic permeability. Data points from different sources are colored differently. Solid lines are a guide to the eye.

5 Connectivity analysis based on complex pore network

The connectivity among nodes with different degrees has been found to play an important role in the transportation and communication within a network. These dependencies can be related to the degree-degree correlations or assortativity, which measures the likelihood that nodes link to nodes of similar or dissimilar nodal degree. The degree correlations can be simply characterized using the degree correlation coefficient r proposed by Newman (2002). It varies between $-1 \le r \le 1$: for $r < 0$ the network is disassortative, for $r = 0$ the network is neutral and for $r > 0$ the network is assortative. Another way to quantify the degree correlations is to measure for each node i the average degree of its neighbors (Pastor-Satorras et al., 2001):

$$k_{nn,i} = \frac{1}{k_i}\sum_{j\in V_i} k_j = \frac{1}{k_i}\sum_{j\in V} A_{ij}k_j \tag{6}$$

where k_i, k_j are the connectivity degree of node *i* and *j*, respectively. Define V as the set of nodes in the complex network, and V_i denote the set of neighbors of node i. A is the adjacency matrix of the complex networks. If node *i* is connected with node *j*, then A_{ij} =1; otherwise, A_{ij} =0.

For all nodes with degree k, $k_{nn}(k)$ is the average degree of the neighbors of all nodes with degree k.

$$k_{nn}(k) = \frac{1}{N_k} \sum_{i \in V_k} k_{nn,i} \tag{7}$$

where V_k is the subset of nodes with degree value equal to k, and $N_k = |V_k|$ is the number of nodes with degree equal to k. A subset of nodes with degree equal to k is more likely to be connected with a subset of nodes with degree equal to $k_{nn}(k)$.

We can inspect the dependence of $k_{nn}(k)$ on k to quantify the degree correlations (Newman, 2002). As shown in **Figure 16**, we discover a slightly overall decreasing trend in $k_{nn}(k)$ for samples 1~3, which indicates nodes of high degree prefer to link with low-degree nodes (see **Figure 11**). For samples 4~7, $k_{nn}(k)$ increases gradually with the increasing degree value, indicating that nodes of comparable degree tend to link to each other, i.e., small-degree nodes to small-degree nodes and hubs to hubs, and the network is called assortative. Thus, the networks for samples 1~3 are disassortative, and networks for samples 4~7 are assortative.

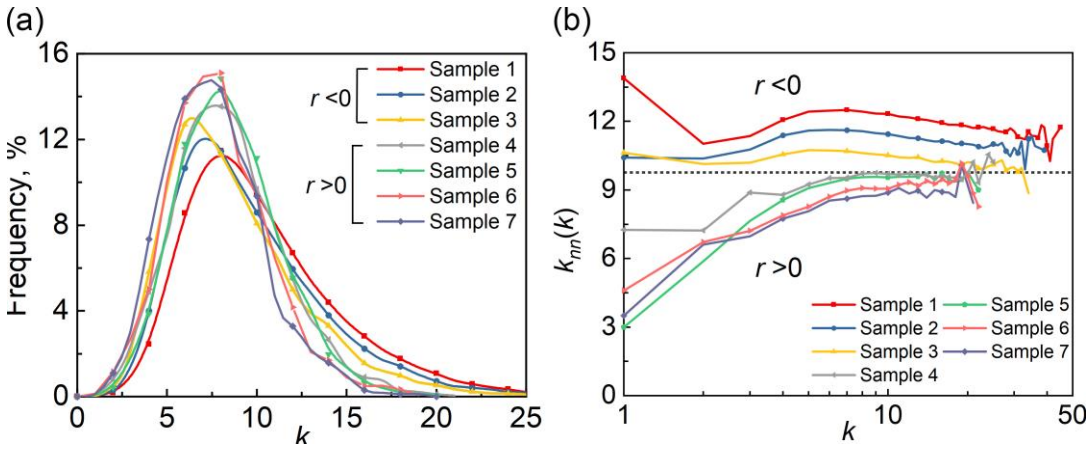

Figure 16 (a) The distributions of nodes degree; (b) The relationships between $k_{nn}(k)$ and node degree.

For disassortative networks (Samples 1~3), the wide and inhomogeneous distributions of node degree implies complicated pore connection patterns. The fluid has a tendency to flow from low-degree pores to high-degree pores. These networks show a scattered and messy distribution of flow paths that results in the flow process tending to be disordered and of high entropy. Thus, more energy will be dissipated during flow, which ultimately leads to low permeability. The assortative networks (Samples 4~7) have relatively simple connection patterns. The flow paths are

relatively regular, and the flow process is in an orderly manner, indicating that less energy will be dissipated and the permeability tends to be high.

Then, we analyze local correlations between the complex network measures of each pore and the pore scale velocity. These measures are summarized in Table 4 and are calculated in terms of the adjacency matrix and node degree, in which A is the adjacency matrix of the graph G with eigenvalue λ; σ_{jk} is the number of paths between node *j* and *k*; $\sigma_{jk}(i)$ is the number of paths between node *j* and *k* that pass through node *i*; λ is the eigenvalue of matrix A. The local clustering coefficient C_i measures the local density of 3-cycles surrounding a node (Watts & Strogatz, 1998). Closeness centrality CC_i is used to describe the importance of a node to transport across the network, which is calculated as the reciprocal of the shortest path length (Bavelas, 1950). A node with high closeness centrality indicates it has close relationships with many nodes (Metcalf & Casey, 2016). Betweenness centrality BC_i is a measure of traffic flow that represents the total fraction of all-pairs shortest paths that pass through node *i* (Brandes, 2001). Eigenvector centrality EC_i describes the qualitative aspect of the connections of node *i*. It is based on the assumption that connections to more critical nodes are more momentous than to less critical nodes (Parau et al., 2017).

Figure 17 shows the correlation matrix of pore scale velocity and measures reflecting node importance. Correlations exist between flow velocity and the node features extracted from complex network analysis, especially the closeness centrality. The results in **Figure 18** suggest that pores with higher closeness centrality have shorter shortest path length and larger flow velocity. On the contrary, pores with lower closeness centrality have longer shortest path length and smaller flow velocity. That is, porous media with more centered pores connected with others make a positive contribution to the fluid flow and show a high permeability. We adopt the closeness centrality of nodes to measure the importance of pore space for fluid flow and reveal the interplay between fluid flow, shortest paths, and pore size in the microcosmic scale.

471 **Table 4** Local parameter calculation formula

Parameter	Variable	Equation
Velocity	V	-
Degree	k	$k_i = \sum_{j=1}^{N} A_{ij}$
Clustering	C	$C_i = \frac{1}{k_i(k_i-1)} \sum_{j,k} A_{ij}A_{jk}A_{ki}$
Closeness centrality	CC	$CC_i = \frac{n-1}{N-1} \frac{n-1}{\sum_{j=1}^{n-1} d_{ij}}$
Betweenness centrality	BC	$BC_i = \frac{2}{(N-1)(N-2)} \sum_{\substack{j,k \in V \\ i \neq j \neq k}} \frac{\sigma_{jk}(i)}{\sigma_{jk}}$
Eigenvector centrality	EC	$EC_i = \frac{1}{\lambda} \sum_{j \in V} A_{ij} \bullet EC_j$

472
473

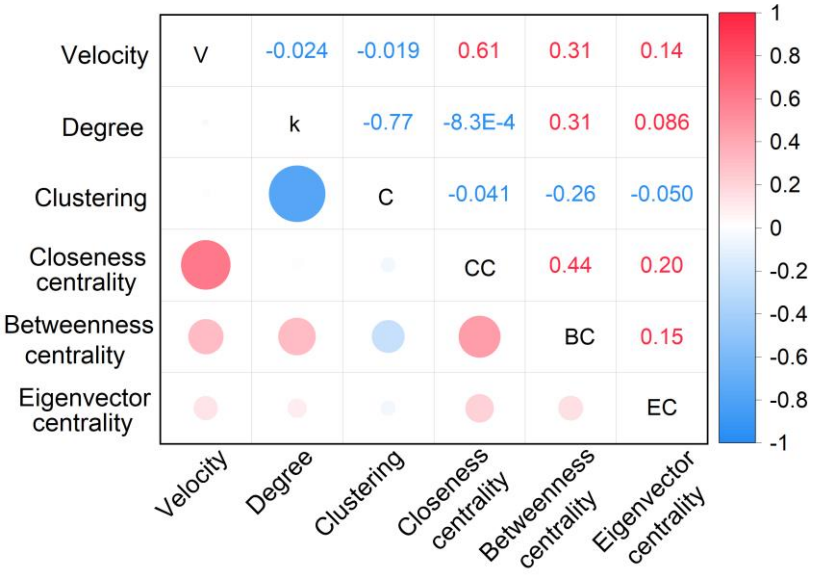

474
475 **Figure 17** Correlation matrix of pore scale velocity and node importance measures of complex
476 network.
477

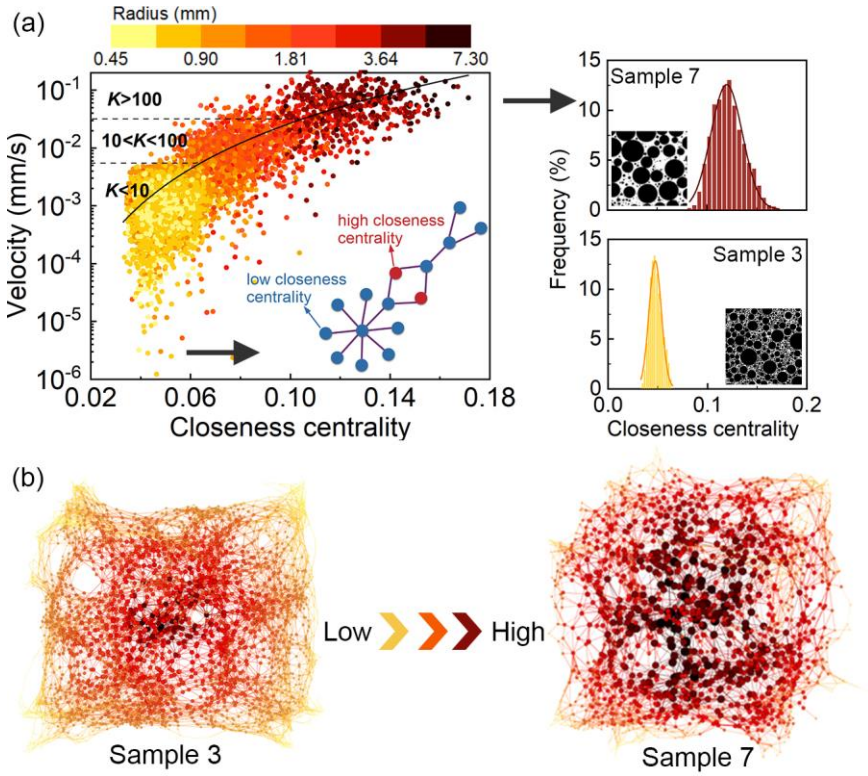

Figure 18 (a) Scatter plots of the node closeness centrality and pore-scale flow velocity and the distributions of the closeness centrality of two granular packings. Dots are colored by pore size; (b) Two typical complex networks. The node size and color depth represent the closeness centrality value.

6 Conclusions

We report a systematic investigation on the influences of pore structure on the flow characteristics of landslide deposits from both micro-and macroscopic perspectives. Seven granular packings with significantly different grain gradations are constructed to represent typical landslide materials. Both pore-space topological measurements and complex network analysis are employed to characterize the pore structure of the idealized landslide materials. The main findings are as follows:

(1) Due to the complex pore structure of landslide materials, there is 1~2 orders of magnitude permeability variation for approximately the same porosity, indicating that porosity alone is not sufficient to determine the macroscopic permeability. The topological characterization of pore structure using tortuosity, heterogeneity, and fractal dimension shows correlation with macroscopic permeability. This is especially evident for pore tortuosity, which demonstrates a

clear relation with permeability that covers eight orders of magnitude for permeability on a variety of porous medium.

(2) The pore network modeling is a powerful tool in analyzing the pore structure of landslide materials. With the increase of coarse grains, the pore throat size becomes larger and the distributions are wider and more heterogeneous, resulting in a high permeability. The pore throat geometry displays clearly three distinctive distributions in the scope of this study. The correspondence between pore throat size distribution and pore connectivity and permeability range suggests the importance of pore size heterogeneity and pore connectivity on the fluid flow. The pore-scale flow velocity and macroscopic permeability show power law growth with throat diameter and its ensemble average value, respectively, with an exponent close to 2, which is in accordance with the Hagen–Poiseuille equation. This means that the relationship between fluid characteristics and complex pore structures is conformed with the simple theory.

(3) The pore space topology is also explored by using complex network approach. The overall measures of complex networks, such as network entropy, global efficiency, and transitivity show significant correlations with macroscopic permeability. The careful inspection of connection patterns between pores reveals that disassortative pore networks have lower permeability and assortative pore networks generally have higher permeability. The closeness centrality is a good measure to link the internal connectivity and the efficiency of transmission pathways across spatial scales.

Acknowledgments

This work was supported by National Key R & D Program of China (No. 2018YFC1508503) and National Natural Science Foundation of China (Grant No. 52179141 & U186520014). The numerical calculations in this work have been done on the supercomputing system in the Supercomputing Center of Wuhan University.

Data Availability Statement

The data supporting this paper can all be found at the corresponding author's github repository (https://github.com/tinazhangjia/Samples-imformation).

References

Ahmadian, M. H., Roohi, E., Teymourtash, A., & Stefanov, S. (2019). A dusty gas model-direct simulation Monte Carlo algorithm to simulate flow in micro-porous media. *Physics of Fluids*, *31*(6). https://doi.org/10.1063/1.5094637

Alim, K., Parsa, S., Weitz, D. A., & Brenner, M. P. (2017). Local Pore Size Correlations Determine Flow Distributions in Porous Media. *Physical Review Letters*, *119*(14), 1–5. https://doi.org/10.1103/PhysRevLett.119.144501

An, S., Yao, J., Yang, Y., Zhang, L., Zhao, J., & Gao, Y. (2016). Influence of pore structure parameters on flow characteristics based on a digital rock and the pore network model. *Journal of Natural Gas Science and Engineering*, *31*, 156–163. https://doi.org/10.1016/j.jngse.2016.03.009

AWAL, R., NAKAGAWA, H., KAWAIKE, K., BABA, Y., & ZHANG, H. (2011). Experimental Study on Piping Failure of Natural Dam. *Journal of Japan Society of Civil Engineers, Ser. B1 (Hydraulic Engineering)*, *67*(4), I_157-I_162. https://doi.org/10.2208/jscejhe.67.i_157

Bavelas, A. (1950). Communication Patterns in Task-Oriented Groups. *The Journal of the Acoustical Society of America*, *22*(6), 725–730. https://doi.org/10.1121/1.1906679

Bernabé, Y., Li, M., & Maineult, A. (2010). Permeability and pore connectivity: A new model based on network simulations. *Journal of Geophysical Research: Solid Earth*, *115*(10), 1–14. https://doi.org/10.1029/2010JB007444

Brandes, U. (2001). A faster algorithm for betweenness centrality. *Journal of Mathematical Sociology*, *25*(2), 163–177. https://doi.org/10.1080/0022250X.2001.9990249

Cai, J., Zhang, Z., Wei, W., Guo, D., Li, S., & Zhao, P. (2019). The critical factors for permeability-formation factor relation in reservoir rocks: Pore-throat ratio, tortuosity and connectivity. *Energy*, *188*, 116051. https://doi.org/10.1016/j.energy.2019.116051

Casagli, N., Ermini, L., & Rosati, G. (2003). Determining grain size distribution of the material composing landslide dams in the Northern Apennines: Sampling and processing methods. *Engineering Geology*, *69*(1–2), 83–97. https://doi.org/10.1016/S0013-7952(02)00249-1

Chen, S. C., Lin, T. W., & Chen, C. Y. (2015). Modeling of natural dam failure modes and downstream riverbed morphological changes with different dam materials in a flume test. *Engineering Geology*, *188*, 148–158. https://doi.org/10.1016/j.enggeo.2015.01.016

Costa, J. E., & Schuster, R. L. (1988). Formation and Failure of Natural Dams. *Bulletin of the Geological Society of America*, *100*(7), 1054–1068. https://doi.org/10.1130/0016-7606(1988)100<1054:TFAFON>2.3.CO;2

Dong, H., & Blunt, M. J. (2009). Pore-network extraction from micro-computerized-tomography images. *Physical Review. E, Statistical, Nonlinear, and Soft Matter Physics*, *80*(3 Pt 2), 36307. https://doi.org/10.1103/PhysRevE.80.036307

Encalada, Á., Barzola-Monteses, J., & Espinoza-Andaluz, M. (2020). A Permeability–Throat Diameter Correlation for a Medium Generated with Delaunay Tessellation and Voronoi Algorithm. *Transport in Porous Media*, *132*(1), 201–217. https://doi.org/10.1007/s11242-020-01387-z

Esmaeilpour, M., Ghanbarian, B., Liang, F., & Liu, H. H. (2021). Scale-dependent permeability and formation factor in porous media: Applications of percolation theory. *Fuel*, *301*(January), 121090. https://doi.org/10.1016/j.fuel.2021.121090

568 Fatt, I. (1956). The Network Model of Porous Media. *Transactions of the AIME*, *207*(01), 144–
569 181. https://doi.org/10.2118/574-g
570 Gerke, K. M., Vasilyev, R. V., Khirevich, S., Collins, D., Karsanina, M. V., Sizonenko, T. O.,
571 Korost, D. V., Lamontagne, S., & Mallants, D. (2018). Finite-difference method Stokes
572 solver (FDMSS) for 3D pore geometries: Software development, validation and case
573 studies. *Computers & Geosciences*, *114*(January), 41–58.
574 https://doi.org/10.1016/j.cageo.2018.01.005
575 Ghanbarian, B., Hunt, A. G., Ewing, R. P., & Sahimi, M. (2013). Tortuosity in Porous Media: A
576 Critical Review. *Soil Science Society of America Journal*, *77*(5), 1461–1477.
577 https://doi.org/10.2136/sssaj2012.0435
578 Gregoretti, C., Maltauro, A., & Lanzoni, S. (2010). Laboratory Experiments on the Failure of
579 Coarse Homogeneous Sediment Natural Dams on a Sloping Bed. *Journal of Hydraulic*
580 *Engineering*, *136*(11), 868–879. https://doi.org/10.1061/(asce)hy.1943-7900.0000259
581 Hormann, K., Baranau, V., Hlushkou, D., Höltzel, A., & Tallarek, U. (2016). Topological
582 analysis of non-granular, disordered porous media: Determination of pore connectivity, pore
583 coordination, and geometric tortuosity in physically reconstructed silica monoliths. *New*
584 *Journal of Chemistry*, *40*(5), 4187–4199. https://doi.org/10.1039/c5nj02814k
585 Huang, Q., Ma, G., Matsushima, T., Zhou, W., & Lin, M. (2021). Effect of disordered pore
586 distribution on the fracture of brittle porous media studied by bonded DEM. *Soils and*
587 *Foundations*, *61*(4), 1003–1017. https://doi.org/10.1016/J.SANDF.2021.05.005
588 Hunt, A. G. (2004). Continuum percolation theory and Archie's Law. *Geophysical Research*
589 *Letters*, *31*(19), 10–13. https://doi.org/10.1029/2004GL020817
590 Jimenez-Martinez, J., & Negre, C. F. A. (2017). Eigenvector centrality for geometric and
591 topological characterization of porous media. *Physical Review E*, *96*(1), 1–13.
592 https://doi.org/10.1103/PhysRevE.96.013310
593 Khirevich, S., Ginzburg, I., & Tallarek, U. (2015). Coarse- and fine-grid numerical behavior of
594 MRT/TRT lattice-Boltzmann schemes in regular and random sphere packings. *Journal of*
595 *Computational Physics*, *281*, 708–742. https://doi.org/10.1016/J.JCP.2014.10.038
596 Lala, A. M. S., & El-Sayed, N. A. A. (2017). Controls of pore throat radius distribution on
597 permeability. *Journal of Petroleum Science and Engineering*, *157*(August), 941–950.
598 https://doi.org/10.1016/j.petrol.2017.08.005
599 Laubie, H., Monfared, S., Radjaï, F., Pellenq, R., & Ulm, F. J. (2017). Disorder-induced stiffness
600 degradation of highly disordered porous materials. *Journal of the Mechanics and Physics of*
601 *Solids*, *106*, 207–228. https://doi.org/10.1016/j.jmps.2017.05.008
602 Laubie, H., Radjai, F., Pellenq, R., & Ulm, F. J. (2017). Stress Transmission and Failure in
603 Disordered Porous Media. *Physical Review Letters*, *119*(7).
604 https://doi.org/10.1103/PhysRevLett.119.075501
605 Li, J. X., Rezaee, R., Müller, T. M., & Sarmadivaleh, M. (2021). Pore Size Distribution Controls
606 Dynamic Permeability. *Geophysical Research Letters*, *48*(5), 1–9.
607 https://doi.org/10.1029/2020GL090558
608 Lindquist, W. B., Venkatarangan, A., Dunsmuir, J. R., & Wong, T. (2000). synchrotron X-ray
609 tomographic images. *Journal of Geophysical Research*, *105*, 509–521.
610 LU, S., LI, J., ZHANG, P., XUE, H., WANG, G., ZHANG, J., LIU, H., & LI, Z. (2018).
611 Classification of microscopic pore-throats and the grading evaluation on shale oil reservoirs.
612 *Petroleum Exploration and Development*, *45*(3), 452–460. https://doi.org/10.1016/S1876-
613 3804(18)30050-8

Ma, G., Zhou, W., Chang, X. L., & Chen, M. X. (2016). A hybrid approach for modeling of breakable granular materials using combined finite-discrete element method. *Granular Matter*, *18*(1), 1–17. https://doi.org/10.1007/s10035-016-0615-3

Metcalf, L., & Casey, W. (2016). Visualizing cybersecurity data. In *Cybersecurity and Applied Mathematics* (pp. 113–134). Syngress. https://doi.org/10.1016/b978-0-12-804452-0.00007-5

Miller, K. J., Montési, L. G. J., & Zhu, W. L. (2015). Estimates of olivine-basaltic melt electrical conductivity using a digital rock physics approach. *Earth and Planetary Science Letters*, *432*, 332–341. https://doi.org/10.1016/j.epsl.2015.10.004

Newman, M. E. J. (2002). Assortative Mixing in Networks. *Physical Review Letters*, *89*(20), 1–4. https://doi.org/10.1103/PhysRevLett.89.208701

Nishiyama, N., & Yokoyama, T. (2017). Permeability of porous media: Role of the critical pore size. *Journal of Geophysical Research: Solid Earth*, *122*(9), 6955–6971. https://doi.org/10.1002/2016JB013793

Okeke, A. C. U., & Wang, F. (2016). Hydromechanical constraints on piping failure of landslide dams: an experimental investigation. *Geoenvironmental Disasters*, *3*(1). https://doi.org/10.1186/s40677-016-0038-9

Ozgumus, T., Mobedi, M., & Ozkol, U. (2014). Determination of kozeny constant based on porosity and pore to throat size ratio in porous medium with rectangular rods. *Engineering Applications of Computational Fluid Mechanics*, *8*(2), 308–318. https://doi.org/10.1080/19942060.2014.11015516

Pang, J., Li, J., Liang, J., Wang, X., & Kui, M. (2018). Evaluation of the percolation sensitivity of loose sandstone using digital core technology. *Open Petroleum Engineering Journal*, *11*, 84–97. https://doi.org/10.2174/1874834101811010084

Papadopoulos, L., Porter, M. A., Daniels, K. E., & Bassett, D. S. (2018). Network analysis of particles and grains. *Journal of Complex Networks*, *6*(4), 485–565. https://doi.org/10.1093/COMNET/CNY005

Parau, P., Lemnaru, C., Dinsoreanu, M., & Potolea, R. (2017). Opinion Leader Detection. In F. A. Pozzi, E. Fersini, E. Messina, & B. B. T.-S. A. in S. N. Liu (Eds.), *Sentiment Analysis in Social Networks* (pp. 157–170). Elsevier. https://doi.org/10.1016/B978-0-12-804412-4.00010-3

Pastor-Satorras, R., Vázquez, A., & Vespignani, A. (2001). Dynamical and correlation properties of the internet. *Physical Review Letters*, *87*(25), 258701-1-258701–258704. https://doi.org/10.1103/PhysRevLett.87.258701

Peng, M., & Zhang, L. M. (2012). Breaching parameters of landslide dams. *Landslides*, *9*(1), 13–31. https://doi.org/10.1007/s10346-011-0271-y

Peters, C. A. (2009). Accessibilities of reactive minerals in consolidated sedimentary rock: An imaging study of three sandstones. *Chemical Geology*, *265*(1–2), 198–208. https://doi.org/10.1016/J.CHEMGEO.2008.11.014

Reichl, L. E., & Luscombe, J. H. (1999). A Modern Course in Statistical Physics, 2nd Edition. *American Journal of Physics*, *67*(12), 1285–1287. https://doi.org/10.1119/1.19118

Russell, S., Walker, D. M., & Tordesillas, A. (2016). A characterization of the coupled evolution of grain fabric and pore space using complex networks: Pore connectivity and optimized flows in the presence of shear bands. *Journal of the Mechanics and Physics of Solids*, *88*, 227–251. https://doi.org/10.1016/j.jmps.2015.12.009

Shabro, V., Torres-Verdín, C., Javadpour, F., & Sepehrnoori, K. (2012). Finite-Difference Approximation for Fluid-Flow Simulation and Calculation of Permeability in Porous Media. *Transport in Porous Media*, *94*(3), 775–793. https://doi.org/10.1007/s11242-012-0024-y

Steinwinder, J., & Beckingham, L. E. (2019). Role of Pore and Pore-Throat Distributions in Controlling Permeability in Heterogeneous Mineral Dissolution and Precipitation Scenarios. *Water Resources Research*, *55*(7), 5502–5517. https://doi.org/10.1029/2019WR024793

Sun, G., Huang, Y., Li, C., & Zheng, H. (2016). Formation mechanism, deformation characteristics and stability analysis of Wujiang landslide near Centianhe reservoir dam. *Engineering Geology*, *211*, 27–38. https://doi.org/10.1016/j.enggeo.2016.06.025

Thomson, P.-R., Aituar-Zhakupova, A., & Hier-Majumder, S. (2018). Image Segmentation and Analysis of Pore Network Geometry in Two Natural Sandstones. *Frontiers in Earth Science*, *6*(June), 1–14. https://doi.org/10.3389/feart.2018.00058

Valera, M., Guo, Z., Kelly, P., Matz, S., Cantu, V. A., Percus, A. G., Hyman, J. D., Srinivasan, G., & Viswanathan, H. S. (2018). Machine learning for graph-based representations of three-dimensional discrete fracture networks. *Computational Geosciences*, *22*(3), 695–710. https://doi.org/10.1007/s10596-018-9720-1

Van Der Linden, J. H., Narsilio, G. A., & Tordesillas, A. (2016). Machine learning framework for analysis of transport through complex networks in porous, granular media: A focus on permeability. *Physical Review E*, *94*(2). https://doi.org/10.1103/PhysRevE.94.022904

van der Linden, J. H., Tordesillas, A., & Narsilio, G. A. (2019). Preferential flow pathways in a deforming granular material: self-organization into functional groups for optimized global transport. In *Scientific Reports* (Vol. 9, Issue 1). https://doi.org/10.1038/s41598-019-54699-6

Wang, Z., Jin, X., Wang, X., Sun, L., & Wang, M. (2016). Pore-scale geometry effects on gas permeability in shale. *Journal of Natural Gas Science and Engineering*, *34*, 948–957. https://doi.org/10.1016/j.jngse.2016.07.057

Watts, D. J., & Strogatz, S. H. (1998). Strogatz - small world network Nature. *Nature*, *393*(June), 440–442. https://www.ncbi.nlm.nih.gov/pubmed/9623998

Xiao, L., Mao, Z. Q., Zou, C. C., Jin, Y., & Zhu, J. C. (2016). A new methodology of constructing pseudo capillary pressure (Pc) curves from nuclear magnetic resonance (NMR) logs. *Journal of Petroleum Science and Engineering*, *147*, 154–167. https://doi.org/10.1016/j.petrol.2016.05.015

Yu, B., & Cheng, P. (2002). A fractal permeability model for bi-dispersed porous media. *International Journal of Heat and Mass Transfer*, *45*(14), 2983–2993. https://doi.org/10.1016/S0017-9310(02)00014-5

Yun, M., Yu, B., & Cai, J. (2009). Analysis of seepage characters in fractal porous media. *International Journal of Heat and Mass Transfer*, *52*(13–14), 3272–3278. https://doi.org/10.1016/j.ijheatmasstransfer.2009.01.024

Zaiser, M. (2017). Porous Materials Exhibit Granular-Like Stress Chains. *Physics*, *10*(August). https://doi.org/10.1103/physics.10.92

Zambrano, M., Tondi, E., & Mancini, L. (2019). *Quantitative pore network analysis and permeability evaluation of porous carbonate reservoir rocks using X-ray computed microtomography images*. *iCT*, 1–6.

Zami-Pierre, F., de Loubens, R., Quintard, M., & Davit, Y. (2018). Effect of disorder in the pore-scale structure on the flow of shear-thinning fluids through porous media. *Journal of Non-*

Newtonian Fluid Mechanics, *261*(August), 99–110. https://doi.org/10.1016/j.jnnfm.2018.08.004

Zhang, L., Xiao, T., He, J., & Chen, C. (2019). Erosion-based analysis of breaching of Baige landslide dams on the Jinsha River, China, in 2018. *Landslides*, *16*(10), 1965–1979. https://doi.org/10.1007/s10346-019-01247-y

Zhang, M., Zhao, H., & Cui, Y. (2021). An innovative image-based workflow for quantitative pore structure characterization in reservoir rocks. *Journal of Petroleum Science and Engineering*, *198*(November 2020), 108179. https://doi.org/10.1016/j.petrol.2020.108179

Zhu, X., Peng, J., Liu, B., Jiang, C., & Guo, J. (2020). Influence of textural properties on the failure mode and process of landslide dams. *Engineering Geology*, *271*(March), 105613. https://doi.org/10.1016/j.enggeo.2020.105613

Zlatić, V., Garlaschelli, D., & Caldarelli, G. (2012). Networks with arbitrary edge multiplicities. *EPL (Europhysics Letters)*, *97*(2), 28005. https://doi.org/10.1209/0295-5075/97/28005